Palaeogeography, Palaeoclimatology, Palaeoecology 637 (2024) 112014

Contents lists available at ScienceDirect

Palaeogeography, Palaeoclimatology, Palaeoecology

journal homepage: www.elsevier.com/locate/palaeo

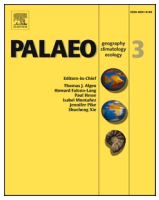

Clumped isotope records of terrestrial temperatures during the Middle Jurassic (180–150 Ma) in East China

Tianjie Jin [a], Katharine W. Huntington [b], Yixiong Wen [c], Xue Gu [a], Andrew J. Schauer [b], Laiming Zhang [a,*]

[a] Frontiers Science Center for Deep-time Digital Earth, State Key Laboratory of Biogeology and Environmental Geology, and School of the Earth Science and Resources, China University of Geosciences, Beijing 100083, China
[b] Department of Earth and Space Sciences, University of Washington, WA 98195-1310, United States
[c] School of Earth Sciences and Engineering, Sun Yat-Sen University, Zhuhai 519082, China

ARTICLE INFO

Editor: Howard Falcon-Lang

Keywords:
Terrestrial paleotemperature
Middle Jurassic
Clumped isotopes
East China

ABSTRACT

The Jurassic is a crucial greenhouse period that witnessed a transition from the relatively colder Triassic to the relatively warmer Cretaceous. However, previous studies based on marine sections suggest different long-term paleotemperature trends throughout the Jurassic. Oxygen isotope ($\delta^{18}O$) values of temperate belemnite and bivalve fossils suggest a general cooling followed by a general warming trend during the Jurassic, whereas TEX_{86}^{H} and clumped isotope sea surface temperature records available for parts of this period appear consistent with a relatively warm and stable climate. The paucity of Middle Jurassic paleotemperature estimates limits efforts to investigate the above disagreement. Here, we apply clumped isotope (Δ_{47}) thermometry to paleosol carbonates from the central part of East China to reconstruct terrestrial paleotemperatures and paleoatmospheric CO_2 (pCO_2) in the Middle Jurassic. After evaluating potential burial diagenesis and seasonality of soil carbonate accumulation, we suggest that terrestrial mean annual temperatures ranged from 30 ± 4 °C to 34 ± 4 °C and the estimated mean pCO_2 was 1219 ± 519 ppmv in mid-latitude East China during the Middle Jurassic. Based on the compiled marine temperatures and our results, we conclude that the paleoclimate was relatively warm and stable from the Middle Jurassic to at least the Earliest Cretaceous (ca. 180–135 Ma). Our estimated Middle Jurassic pCO_2 aligns with previous records, revealing minimal variations compared to the pCO_2 observed during the Early Cretaceous. These findings imply a link between the consistent temperatures and the relatively stable pCO_2 levels from the Middle Jurassic through the Early Cretaceous.

1. Introduction

As a typical greenhouse climate period with high atmospheric CO_2 concentrations (pCO_2) (Berner and Kothavala, 2001; Fletcher et al., 2008), the Jurassic saw the transition from relative cold paleoclimate during the Triassic (Berner and Kothavala, 2001; Price et al., 2013) to extreme warmth during the Cretaceous (O'Brien et al., 2017; Huber et al., 2018). This profound shift has led several studies to investigate paleotemperature evolution during the Jurassic as an analog for contemporary climate warming. Based on the oxygen isotope ($\delta^{18}O$) values of temperate belemnite and bivalve fossils, previous studies have suggested a general cooling of sea surface temperatures (SSTs) during the Early-Middle Jurassic followed by a general warming trend during the Late Jurassic (Dera et al., 2011; Grossman, 2012). In contrast, recent SST reconstructions at both middle and high latitudes based on TEX_{86} (Jenkyns et al., 2012) and clumped isotope thermometry (Vickers et al., 2019; Letulle et al., 2022) point to relatively warm and stable paleoclimate (i.e., 25–30 °C) with occasional cooling events during the Jurassic. The largest discrepancy between these records occurs in the Early to Middle Jurassic, where sparse SST data show no major change despite a 4‰ shift in $\delta^{18}O$ values, which could represent up to >15 °C of temperature change (Grossman, 2012). The lack of temperature estimates during the Middle Jurassic and the disagreement among multiple proxies limit our understanding of the Jurassic paleoclimate and the cool-to-warm transition.

At present, Jurassic paleotemperature reconstructions are mainly

* Corresponding author at: State Key Laboratory of Biogeology and Environmental Geology, China University of Geosciences, Beijing and School of the Earth Science and Resources, China University of Geosciences, Beijing 100083, China.
E-mail address: lzhang@cugb.edu.cn (L. Zhang).

https://doi.org/10.1016/j.palaeo.2024.112014
Received 29 June 2023; Received in revised form 7 November 2023; Accepted 2 January 2024
Available online 5 January 2024

based on marine sections, while terrestrial paleotemperatures are less reported (Shen et al., 2021). Yet there is potential for terrestrial reconstructions to illuminate these trends, as marine and terrestrial paleoproxy data show similar trends and temperatures (within 3 °C) at middle latitudes during warm paleoclimatic conditions (Zhang et al., 2019; Joachimski et al., 2022). For example, terrestrial paleotemperatures from NE China during the Late Cretaceous show good consistency with global marine records (Wang et al., 2013; Zhang et al., 2018). These observations suggest the potential for terrestrial paleotemperature reconstructions from similar paleogeographic locations to complement the Middle Jurassic global sea surface paleotemperature curve and shed new light on the Jurassic paleoclimate evolution.

In this study, we apply clumped isotope (Δ_{47}) thermometry to paleosol carbonates from East China to estimate mid-paleolatitude terrestrial paleotemperatures during the Middle Jurassic. Our targets are well-exposed and effectively temporally constrained Jurassic strata that contain abundant paleosol carbonates that are suitable for terrestrial paleotemperature reconstruction (Li et al., 2012; Meng et al., 2019; Li et al., 2020; Shen et al., 2021; Zhang et al., 2021; Dai et al., 2022). We rigorously evaluate sample preservation and possible recrystallization and/or solid-state reordering of the clumping signal by burial diagenesis. We then interpret isotopic results for well-preserved samples, accounting for the seasonality of soil carbonate accumulation. The results allow us to test the hypothesis that temperature in East China remained relatively warm and stable from the Early to Late Jurassic during the interval of significant variation in the $\delta^{18}O$ curve. Comparison of the reconstructed terrestrial mean annual temperatures with a compilation of Jurassic-Early Cretaceous marine paleotemperatures enables us to refine our interpretation of the terrestrial paleoclimatic characteristics during the Middle Jurassic and may provide new constraints on Jurassic-Early Cretaceous paleotemperature evolution. In addition, we estimate pCO_2 from carbon isotopes of paleosol carbonates and compare them to the reported pCO_2 records during the Jurassic-Early Cretaceous, which allow us to examine the links between pCO_2 and paleotemperature records.

2. Stratigraphy and sampling

Both paleogeographic reconstructions and paleomagnetism studies indicate that East China stabilized at middle latitudes during the Jurassic with no major latitudinal changes (Scotese, 2014; Huang et al., 2018; Gao et al., 2021) (Fig. 1A). The central part of East China contains many terrestrial basins with well-preserved Mesozoic strata (Huang, 2019; Li et al., 2012; Meng et al., 2019) (Fig. 1B). In these basins,

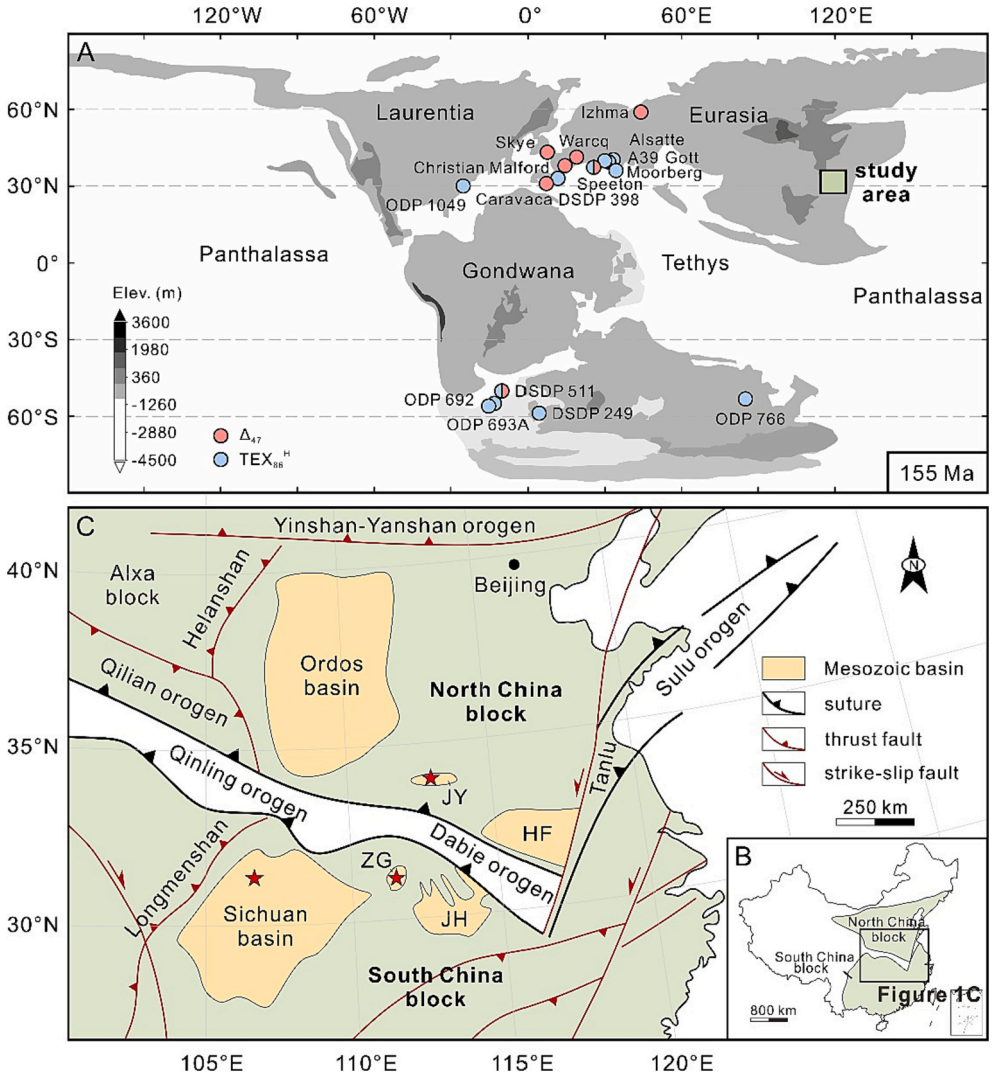

Fig. 1. Paleogeographic reconstruction for the Middle Jurassic (155 Ma). (A) Paleogeographic map modified from Scotese (2014) to show the locations of our study area (green rectangle) and the compiled Jurassic-Early Cretaceous marine temperature records based on Δ_{47} (red circles) and TEX_{86}^{H} paleothermometry (blue circles). (B) Sketched structural map of China. (C) Simplified geological map of middle East China showing the locations of the sampled sections (red stars) (modified after Li et al., 2012). (For interpretation of the references to colour in this figure legend, the reader is referred to the web version of this article.)

numerous paleosols developed in fluvial-lacustrine sections and contain abundant carbonate nodules. Most paleosols are reddish and brownish, with a minority being yellowish (Fig. S1). Paleosol nodules are generally ginger-like and irregular in shape, and the diameters are generally 2–5 cm (Fig. S2). All the paleosols in this study are defined as aridisol following the general classification of paleosols by Retallack (2001).

Here, we collected paleosol carbonates from three non-intermontane basins with low paleoelevations during the Middle Jurassic (Huang, 2019; Meng et al., 2019), including the Sichuan Basin and Zigui Basin (South China block), and the Jiyuan Basin (North China block) (Fig. 1C). For each section, multiple carbonate nodules were collected from multiple paleosol layers to obtain representative paleoproxy data from the paleosol carbonates.

2.1. The Sichuan Basin

The Sichuan Basin is an extensive superimposed basin that occupies an area of ~1.8 × 10^5 km^2 in the northwest of the South China block (Meng et al., 2005; Huang, 2019) (Fig. 1C). During the Jurassic, its paleolatitude was ~37°N (van Hinsbergen et al., 2015). The Jurassic strata are characterized by fluvial-lacustrine purplish red clastic rocks (Li et al., 2020; Li et al., 2018). In ascending order, they are divided into the Ziliujing Formation (J_1z), Qianfoya Formation (J_2q), Shaximiao Formation (J_2s), Suining Formation (J_3s), and Lianhuakou Formation (J_3l) (Meng et al., 2005) (Fig. 2A).

In the Guangyuan area in the northwest Sichuan Basin (105°43′58″E, 32°23′38”N), we collected carbonate nodules (>30 cm below the paleosol surfaces) from the Qianfoya, Shaximiao, Suining, and Lianhuakou Formations (Fig. 2A). Based on sporopollenin and bivalve assemblages, the Qianfoya and Shaximiao Formations are Aalenian-Bajocian and Bathonian-Callovian in age, respectively (Meng et al., 2005; Deng et al., 2017). Previous biostratigraphic studies indicate that the Suining and Lianhuakou Formations are Oxfordian and Kimmeridgian in age, respectively (Deng et al., 2017).

2.2. The Zigui Basin

The Zigui Basin, situated to the east of the Sichuan Basin, contains a Jurassic terrestrial sequence that is nearly identical to that of the Sichuan Basin (Liu et al., 2005; Dai et al., 2022) (Fig. 1C). During the Jurassic, its paleolatitude was ~38°N (van Hinsbergen et al., 2015). The Jurassic strata mainly consist of red mudstones and variably colored sandstones and siltstones (Dai et al., 2022). In ascending order, they are divided into the Tongzhuyuan Formation (J_1t), Qianfoya Formation (J_2q), Shaximiao Formation (J_2s), Suining Formation (J_3s), and Penglaizhen Formation (J_3p) (Dai et al., 2022) (Fig. 2B).

In Zigui County (110°39′18″E, 31°5′30”N), we collected carbonate nodules (>30 cm below the paleosol surfaces) from the Qianfoya, Shaximiao, and Penglaizhen Formations (Fig. 2B). Biostratigraphic constraints indicate that the Qianfoya Formation is Aalenian-Bajocian in age, and the Shaximiao Formation is Bathonian-Callovian in age, and thus are temporally comparable to the same units in the Sichuan Basin (Dai et al., 2022). A Kimmeridgian age has been proposed for the Penglaizhen Formation, making it contemporaneous with the Lianhuakou Formation in the Sichuan Basin (Deng et al., 2017).

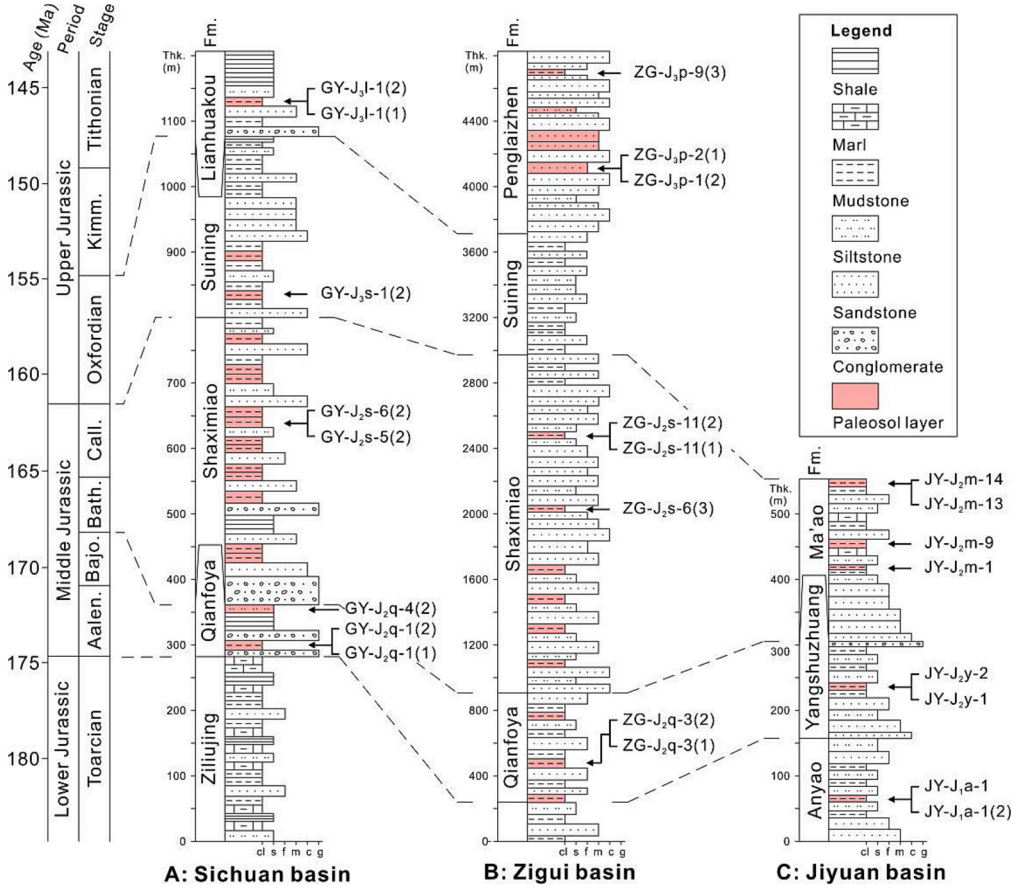

Fig. 2. Stratigraphic columns showing the Jurassic strata of (A) the Sichuan Basin, (B) the Zigui Basin, and (C) the Jiyuan Basin. The black arrows indicate the samples for clumped isotope analyses. The dashed lines show temporally comparable strata. cl = clay; s = silt; f = fine sand; m = medium sand; c = coarse sand; g = granules.

2.3. The Jiyuan Basin

The Jiyuan Basin is situated to the north of the Zigui Basin (Fig. 1C). During the Jurassic, its paleolatitude was ~40°N (van Hinsbergen et al., 2015). The Jurassic strata are composed of grey-yellow-green fluvial-lacustrine sandstones, siltstones, and mudstones (Yang et al., 2014; Wang et al., 2019). In ascending order, they are divided into the Anyao Formation (J_1a), Yangshuzhuang Formation (J_2y), and Ma'ao Formation (J_2m) (Fig. 2C).

From the Jiyuan area (112°29′10″E, 35°4′4"N), we collected carbonate nodules (>30 cm below the paleosol surfaces) from the Anyao, Yangshuzhuang, and Ma'ao Formations (Fig. 2C). The Anyao Formation is Toarcian in age (Yang et al., 2014; Deng et al., 2017). Based on bivalve assemblages of *Unio-Margaritifera-Yananoconcha-Ferganoconcha*, the Yangshuzhuang Formation is Aalenian-Bajocian in age (Huang, 2019). Ostracod assemblages of *Timiriasevia-Darwinula* indicate that the Ma'ao Formation is Bathonian-Callovian in age (Yang et al., 2014; Deng et al., 2017).

3. Methods

3.1. Petrographic analysis

All the carbonate nodules were carefully assessed for diagenesis using cathodoluminescent (CL) microscopy. The optical and CL observations were conducted using a Cathodoluminescence Mk5–2 instrument, operating at 5–10 kV, 0.5 mA, and 50–100 mTorr. According to the luminescent properties, our samples are categorized as non-luminescent (NL), slightly luminescent (SL), and mostly luminescent (ML) (Fig. S2). Nodules were assigned to the NL category if they were characterized by homogenous micrite with a low luminescence and not a single detrital carbonate grain was observed. Nodules consisting mainly of micrite with isolated brighter specks or veins were assigned to the SL category, while those containing pervasively luminescent spars or veins were assigned to the ML category.

3.2. Carbonate clumped isotope analysis

Carbonate clumped isotope thermometry relies on the thermodynamic tendency of heavy isotopes to "clump" into bonds with each other rather than with light isotopes in carbonate minerals (Ghosh et al., 2006; Eiler, 2007; Huntington and Petersen, 2023). The mass-47 anomaly (Δ_{47}) measured in carbonate-derived CO_2 quantifies the abundance of clumped, or multiply-substituted ion groups containing more than one heavy isotope (mostly mass-47 $^{13}C^{18}O^{16}O$), relative to the expected abundance in a random distribution. The abundance of $^{13}C^{18}O^{16}O$ in the carbonate increases with decreasing growth temperature, and thus Δ_{47} provides a direct means to estimate the growth temperature of carbonate without estimating the $\delta^{18}O$ of soil water ($\delta^{18}O_{sw}$) (Eiler, 2007). The Δ_{47}, $\delta^{13}C$, and $\delta^{18}O$ are measured simultaneously, which enables the estimate of the $\delta^{18}O_{sw}$.

About 60–80 mg of powder was drilled from the polished surfaces of the nodules using a slow dental drill under a binocular microscope. For each nodule, all the drilled carbonate powder was thoroughly homogenized. Clumped isotope analyses (24 samples; 2–4 replicates for each sample) were conducted at the IsoLab at the University of Washington (Seattle, USA). The analysis followed the methods described in Burgener et al. (2016) and Schauer et al. (2016). For each analysis, a pure carbonate equivalent sample weighing 8–10 mg was subjected to digestion in a 90 °C common phosphoric acid bath for 10 min to obtain CO_2. The generated CO_2 was separated from water using cryogenic methods and subsequently purified. The purified CO_2 was sealed in a quartz tube and then introduced into a Thermo MAT253 mass spectrometer configured to measure *m/z* 44–49 inclusive for analysis. Between every 4–5 sample unknowns, equilibrated CO_2 reference gases and carbonate standards were included in the analysis sequence. The carbonate Δ_{47} values were calibrated to the carbon dioxide equilibration scale (CDES) using CO_2 gases isotopically equilibrated at 4, 60, and 1000 °C (Dennis et al., 2011). The laboratory carbonate standards (C2, C64, Coral, ETH1, ETH2, ETH3, and ETH4) exhibited a long-term standard deviation (SD) of 0.027‰. The T(Δ_{47}) values were calculated using the calibrations provided by Kelson et al. (2017), Petersen et al. (2019), and Anderson et al. (2021) in Table S1. The discrepancies among these three calibrations are ≤3 °C, and there is no impact on the temperature trend. In this study, we adopted the values obtained through the Anderson et al. (2021) equation. This equation stands out for its rigorously replicated and standardized calibration, and it is suitable for a wide range of temperature and sample types (Huntington and Petersen, 2023). The oxygen isotopic composition of soil water ($\delta^{18}O_{sw}$) in equilibrium with the measured carbonate nodule $\delta^{18}O$ at the observed apparent T(Δ_{47}) was calculated using the carbonate-water oxygen isotope fractionation relation of Kim and Oneil (1997). The $\delta^{13}C$ and $\delta^{18}O$ values are reported relative to either the Vienna Peedee belemnite (VPDB) for minerals or Vienna standard mean ocean water (VSMOW) for water.

3.3. Assumptions and methods of atmospheric CO_2 estimation

We used the pedogenic carbonate barometer described in Cerling (1991) to estimate the pCO_2:

$$C_a = S_{(z)} \times \left(\delta^{13}C_s - 1.0044\delta^{13}C_r - 4.4\right) / \left(\delta^{13}C_a - \delta^{13}C_s\right)$$

where C_a is the atmospheric CO_2 (ppmv), $S_{(z)}$ is the soil-respired CO_2 concentration, and $\delta^{13}C_s$, $\delta^{13}C_r$, and $\delta^{13}C_a$ are the stable carbon isotopic compositions of soil CO_2, soil-respired CO_2, and atmospheric CO_2, respectively.

The $\delta^{13}C_s$ was calibrated by the carbon isotopic composition of pedogenic carbonate ($\delta^{13}C_c$) following the temperature-dependent equation $\delta^{13}C_s = (\delta^{13}C_c + 1000)/[(11.98–0.12\ T)/1000 + 1] - 1000$ (Romanek et al., 1992), where we used Δ_{47}-derived temperatures in this study to represent T. The $\delta^{13}C_r$ was calculated from the organic matter ($\delta^{13}C_o$) in paleosol using the equation $\delta^{13}C_r = \delta^{13}C_o - 1$ (Breecker and Retallack, 2014). In this study, we used contemporary $\delta^{13}C_o$ from the Sichuan Basin (Li et al., 2022a, 2022b) to calculate $\delta^{13}C_r$ for the Sichuan Basin and the Zigui Basin, and from the Ordos Basin (Jin et al., 2020) to calculate $\delta^{13}C_r$ for the Jiyuan Basin. The $\delta^{13}C_a$ was calibrated from $\delta^{13}C_o$ using the equation $\delta^{13}C_a = (\delta^{13}C_o + 18.67)/1.1$ (Arens et al., 2000). Finally, the $S_{(z)}$ was estimated as a constant value of 2000 ppmv for our samples that collected >30 cm below the paleosol surfaces, which is suggested for semi-arid areas as the calcisols are reddish-brownish aridisols. Besides, Li et al. (2022a, 2022b) reported that the $S_{(z)}$ derived from original depth to carbonate nodules and corrected for compaction in paleosols was around 2000 ppmv in the Sichuan Basin during the Middle Jurassic. The standard errors of C_a were calculated using the Gaussian approach (Breecker and Retallack, 2014).

3.4. Global marine temperature and pCO_2 compilation

To contextualize our results, we compiled published Jurassic-Early Cretaceous (180–120 Ma) marine temperatures interpreted to represent sea surface conditions based on Δ_{47} and TEX_{86} paleothermometry. In this study, only samples reflecting primary temperatures from mid-paleolatitudes of 30°-60°N/S (similar to our study areas) are included (see Fig. 1A for the locations). The compilation consists of 52 Δ_{47}-derived temperatures and 265 TEX_{86}-derived temperatures (Table S2). We calculated the stage mean values for Δ_{47}-derived SSTs according to their original published age (Table S2). The TEX_{86}-derived temperatures were calculated using the TEX_{86}^{H} calibration since this logarithmic calibration is generally recommended for warm conditions (i.e., SSTs >15 °C) (Kim et al., 2010).

We also compiled published Jurassic-Early Cretaceous (180–120 Ma) global pCO_2 records based on pedogenic carbonates and stomatal

characters of fossil plants. The compilation consists of 24 pedogenic carbonate-based pCO_2 records and 25 stomata-based pCO_2 records. We updated the pedogenic carbonate-based pCO_2 records using the equations described in Section 3.4 with $T = 30$ °C and $S_{(z)} = 2000$ ppmv (see Table S3 for details).

4. Results

4.1. Clumped and bulk isotope results and CL observations

The clumped isotope data (Δ_{47}, $\delta^{13}C$, and $\delta^{18}O$), as well as $T(\Delta_{47})$ and $\delta^{18}O_{sw}$, are summarized in Table S1. The average Δ_{47} values for NL nodules ($n = 7$) range from 0.560‰ to 0.593‰ (CDES, 90 °C acid digestion reference frame), corresponding to apparent $T(\Delta_{47})$ values ranging from 25 ± 5 °C to 37 ± 6 °C (1 SE) (Fig. 3; Table S1). Their $\delta^{18}O$ and $\delta^{13}C$ values range from −9.8‰ to −7.1‰ and from −12.5‰ to −4.2‰ VPDB, respectively (Table S1). The calculated $\delta^{18}O_{sw}$ values range from −6.3‰ to −4.2‰ VSMOW, in the plausible range for soil water (Table S1). All the apparent $T(\Delta_{47})$ values are within the Earth's surface temperature range (<40 °C). Moreover, the optical and CL features of the NL nodules (i.e., dense and homogeneous micrites) show no sign of recrystallization.

The average Δ_{47} values for SL and ML nodules ($n = 16$) range from 0.346‰ to 0.551‰, corresponding to apparent $T(\Delta_{47})$ values ranging from 41 ± 5 °C to 76 ± 9 °C (1 SE) (Fig. 3; Table S1). Their $\delta^{18}O$ and $\delta^{13}C$ values range from −13.2‰ to −3.6‰ and from −9.1‰ to −2.5‰ VPDB, respectively (Table S1). The calculated $\delta^{18}O$ values of water that would be in equilibrium with these carbonate samples at the apparent T (Δ_{47}) range from −7.7‰ to 3.5‰ VSMOW (Table S1). All the $T(\Delta_{47})$ values are above the Earth-surface temperature range (<40 °C). Post-depositional water-rock interaction can change carbonate bulk stable isotope compositions in a fluid-buffered system, but may not change them in a rock-buffered system (Banner and Hanson, 1990). If the alteration occurred at elevated temperatures during burial, the carbonate Δ_{47} values would yield higher apparent temperatures than that of its original depositional environment (Ingalls and Snell, 2021). Therefore, we conclude that the SL and ML nodules were altered by fluid-mediated reactions including significant material addition during burial diagenesis, and exclude these altered samples from further discussion.

4.2. Global marine temperature records

The compiled mid-paleolatitude (30°-60°N/S) marine temperatures based on Δ_{47} and TEX_{86}^{H} estimates are summarized in Table S2. The Δ_{47}-derived temperatures are only available during ca. 165–150 Ma and around ca. 186 Ma during the Jurassic, and ca. 125–135 Ma during the Early Cretaceous. According to the habitat of the analyzed marine species, they reflect surface water temperatures and range from 18.7 ± 4.6 °C to 31.9 ± 4.4 °C (Price et al., 2020; Vickers et al., 2019, 2020, 2021; Letulle et al., 2022) (Table S2). The calculated mean temperatures for each stage range from 19.0 ± 7.0 °C to 27.8 ± 4.3 °C (1 standard error of the mean, SE; Table S2).

The TEX_{86}^{H}-derived temperature data are relatively continuous from the Late Jurassic (Jenkyns et al., 2012) to the Early Cretaceous (O'Brien et al., 2017 and references therein; Cavalheiro et al., 2021), but are lacking during the Early-Middle Jurassic. From the Late Jurassic to the Early Cretaceous, the compiled TEX_{86}^{H}-derived sea surface temperatures (SSTs) range from 21.9 ± 2.5 °C to 37.1 ± 2.5 °C (Table S2).

4.3. CO_2 concentrations

The pCO_2 values estimated by carbon isotope ratios of the paleosol nodules in the central part of East China, along with compiled global pCO_2 records, are summarized in Table S3. Our estimated pCO_2 values range from 1368 to 1561 ppmv, except for one extremely low value of 303 ppmv. The average pCO_2, when taking all the values into account, is 1219 ± 519 ppmv (Table S3). When excluding the extremely low value, the average pCO_2 becomes 1525 ± 633 ppmv. The difference between these two estimates falls within the errors of the pCO_2 calculations. Nevertheless, we suggest that 1219 ± 519 ppmv is more reasonable, as the $T(\Delta_{47})$ value corresponding to the sample with low pCO_2 is primary, and thus there is no compelling reason to exclude it.

The compiled pedogenic carbonate-based pCO_2 records range from 621 to 2170 ppmv, with a mean value of 1163 ppmv during the Jurassic and 1046 ppmv during the Early Cretaceous (Ekart et al., 1999; Huang et al., 2012; Li et al., 2020; Li et al., 2022a, 2022b). The pCO_2 records derived from stomatal characters of fossil plants range from 400 to 4020 ppmv, with a mean value of 1521 ppmv during the Jurassic and 1754 ppmv during the Early Cretaceous (Sun et al., 2007; Retallack, 2009; Yan et al., 2009; Wu et al., 2016; Li et al., 2020) (Table S3).

5. Discussion

In the following sections, we evaluate possible solid-state reordering effects on the Δ_{47} values of the NL nodules, which cannot be detected by petrographic analyses (Huntington and Lechler, 2015; Ingalls and Snell, 2021). We then interpret our Δ_{47}-derived terrestrial temperatures in the

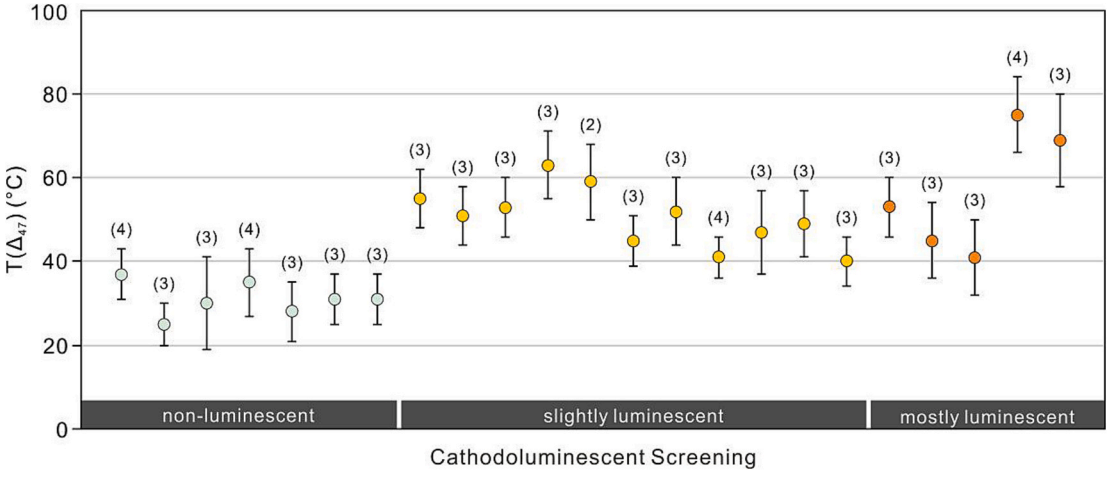

Fig. 3. The $T(\Delta_{47})$ results in this study. They are categorized as non-luminescent (NL), slightly luminescent (SL), or mostly luminescent (ML) based on the luminescent properties of the carbonate nodules. Numbers of replicates are reported in parentheses. The sample-level error bars represent 1 standard error (1SE) of the mean based on internal replicates or external instrument precision, whichever is larger (see Table S1 for the calculation of error).

context of seasonally biased soil carbonate accumulation and compare them with the compiled marine temperatures to further assess the reliability of our estimates.

5.1. Evaluation of possible solid-state reordering effects

As we discussed in Section 4.1, petrographic observations exclude the scenario in which the NL nodules experienced obvious pervasive recrystallization or precipitation of diagenetic carbonate (Fig. S2). However, carbonate nodules can also be affected by solid-state reordering due to burial heating, which would alter Δ_{47} values at elevated temperatures without changing mineral textures (Huntington and Lechler, 2015; Ingalls and Snell, 2021). Here, we further explore the potential for this type of alteration using solid-state reordering models (Henkes et al., 2014; Stolper and Eiler, 2015; Hemingway and Henkes, 2021) and temperature history constraints for the units that contain NL nodules, the Anyao Formation in the Jiyuan Bain, Qianfoya Formation in the Zigui Basin, and Shaximiao and Suining formations in the Sichuan Basin.

For each Formation, its depositional age and thermal history are constrained to define a suite of possible representative post-depositional time-temperature (t-T) paths (Fig. 4). Then the t-T paths and a range of possible initial depositional temperatures (T_0) are used to simulate sample Δ_{47} values and assist in assessing the likelihood that original depositional T(Δ_{47}) values were altered by solid-state reordering. Fig. 4 shows model results for two cases of T_0, assuming depositional temperature equal to either the analyzed T(Δ_{47}) value or a nominal surface temperature of 20 °C (see Supplemental Fig. S2 for additional scenarios), and a modern mean annual Earth-surface temperature (T_{final}) of 20 °C (results are indistinguishable using 15 °C). The calculations and figures are output from the open source "isotopylog" package (Hemingway, 2020; http://pypi.python.org/pypi/isotopylog), including models from Henkes et al. (2014) (Hea14 model, hereafter), Stolper and Eiler (2015) (SE15 model, hereafter), and Hemingway and Henkes (2021) (HH21 model, hereafter).

For the Jiyuan Basin, based on modeling of low-temperature thermochronology data, the Anyao Formation reached a maximum burial temperature (T_{max}) of ca. 115 °C during the Late Cretaceous, then decreased to a near-surface temperature of 20 °C during the Late Cretaceous-Paleocene (Zhao et al., 2002). Here we set the T_{max} to 115 °C at 90 Ma (Fig. 4A–C). For the Zigui Basin (Fig. 4D–F), apatite fission-track thermochronological data indicated that the burial temperature of the Qianfoya Formation rapidly increased to 120 °C (T_{max}) at ca. 120 Ma, then decreased to 60 °C at 80 Ma, and finally decreased to a near-surface temperature (i.e., 20 °C) no earlier than 20 Ma (Yu et al., 2017). For the Sichuan Basin (Fig. 4G–L), the t-T paths of the Jurassic strata are well-constrained by modeling of low-temperature thermochronology data (Shi et al., 2016). The burial temperature of the Shaximiao Formation quickly increased to 120 °C (T_{max}) at 130 Ma then quickly decreased to 55 °C at 90 Ma. After that, it slowly decreased to 50 °C at 90–15 Ma and finally decreased to a near-surface temperature. The burial temperature of the Suining Formation reached a T_{max} of 110 °C at 110 Ma, then quickly decreased to 65 °C at 80 Ma. After that, it slowly decreased to 56 °C at 80–30 Ma and finally decreased to a near-surface temperature.

For the Hea14 model and HH21 model, the final predicted temperatures for all NL samples show no significant effect of solid-state reordering (i.e., < 0.1 °C effect on T(Δ_{47}) for all the thermal history scenarios (Fig. 4). For the SE15 model, the final predicted apparent T(Δ_{47}) values are ca. 30 °C higher than T_0; however, this result is incompatible with our observations, suggesting that the SE15 model is not suitable for our samples. In the SE15 model, the final modeled temperatures for each Formation are higher than our measured T(Δ_{47}) values even if we set T_0 to 0 °C (Fig. S3). Matching our observed temperatures would require mean annual temperature and soil carbonate accumulation below 0 °C, which is not compatible with low-elevation, mid-latitude regions during the greenhouse Jurassic. All of the other model results support the interpretation that the NL nodules were not altered by solid-state reordering and faithfully archive Jurassic Earth-surface temperatures.

5.2. Evaluation of soil carbonate seasonality

The T(Δ_{47}) values obtained from NL carbonate nodules represent the growth temperatures of the paleosol carbonates. However, these values can be influenced by precipitation seasonality, soil texture, and vegetation cover, which may introduce a bias towards soil carbonate accumulation in different seasons (e.g., Passey et al., 2010; Peters et al., 2013; Kelson et al., 2020). We therefore assess the likely seasonality of precipitation and soil moisture balance relevant for the sampled soil nodules. Recent high-resolution climate simulations suggest that the central part of East China would receive the majority of precipitation from April to September during the Jurassic (Li et al., 2022a, 2022b). Our paleosol nodules were sampled from mudstones and siltstones, indicating they formed in a fine-grained soil matrix (Section 2). Fine-grained soils have good moisture retention ability and may delay soil drying, such that carbonate in summer rainy season climates may be expected to accumulate in autumn, when soil temperatures approach mean annual temperature (Gallagher and Sheldon, 2016). We therefore interpret our Jurassic T(Δ_{47}) values of 25 ± 5 °C to 37 ± 6 °C from the NL nodules to represent terrestrial mean annual temperatures—an interpretation that is broadly consistent with previous paleontological and sedimentological studies suggesting high mean annual temperature in East China during the Jurassic (Wang, 2002; Deng et al., 2017).

5.3. Warm and stable terrestrial paleotemperature in East China during the Middle Jurassic

To obtain a robust mean temperature for each period, we integrate data for NL nodules from time-equivalent units. In this study, mean temperatures for the Toarcian, Aalenian-Bajocian, Bathonian-Callovian, and Oxfordian are calculated by averaging the Δ_{47} values of all replicates within NL strata of these ages, respectively (Table S1). For the late Early Jurassic (Toarcian), the Δ_{47} values of individual nodules range from 0.560‰ to 0.593‰, corresponding to apparent T(Δ_{47}) values ranging from 25 ± 5 °C to 37 ± 6 °C (1 SE), with a representative mean temperature of 32 ± 4 °C (1 SE). For the early Middle Jurassic (Aalenian-Bajocian), the Δ_{47} values for individual nodules range from 0.565‰ to 0.580‰, corresponding to apparent T(Δ_{47}) values ranging from 30 ± 11 °C to 35 ± 8 °C (1 SE), with a representative mean temperature of 33 ± 6 °C (1 SE). For the late Middle Jurassic (Bathonian-Callovian), the Δ_{47} values for individual nodules range from 0.577‰ to 0.586‰, corresponding to apparent T(Δ_{47}) values ranging from 28 ± 7 °C to 31 ± 6 °C (1 SE), with a representative mean temperature of 29 ± 4 °C (1 SE). For the early Late Jurassic (Oxfordian), the Δ_{47} value is 0.577‰ and yields an apparent T(Δ_{47}) value of 31 ± 6 °C (1 SE). To sum up, representative mean temperatures for the late Early-early Late Jurassic in the central part of East China range from 29 ± 4 °C to 33 ± 6 °C (1 SE).

To facilitate the comparison of datasets from different locations, we next correct the representative time-period mean temperatures from our terrestrial sections to the same paleolatitude (i.e., 35° N) by applying a latitudinal temperature gradient. Constraints on marine latitudinal gradients exist for the Jurassic, ranging from 0.26 ± 0.05 °C/° at middle and high latitudes during the Early Jurassic (Letulle et al., 2022) to 0.2 to 0.5 °C/° during the Middle-Late Jurassic (Dromart et al., 2003). A synthesis of paleoproxy data by Zhang et al. (2019) showed that latitudinal temperature gradients for terrestrial and marine environments are similar for other past warm periods (e.g., latest Cretaceous, ~0.4 °C/° for both ocean and continent; Amiot et al., 2004). Consistent with these findings, we adopt a latitudinal temperature gradient of 0.4 ± 0.1 °C/° and the corrected time-period mean temperatures range from 30 ± 4 °C to 34 ± 4 °C (Figs. 5 and 6; for error propagation see Table S1).

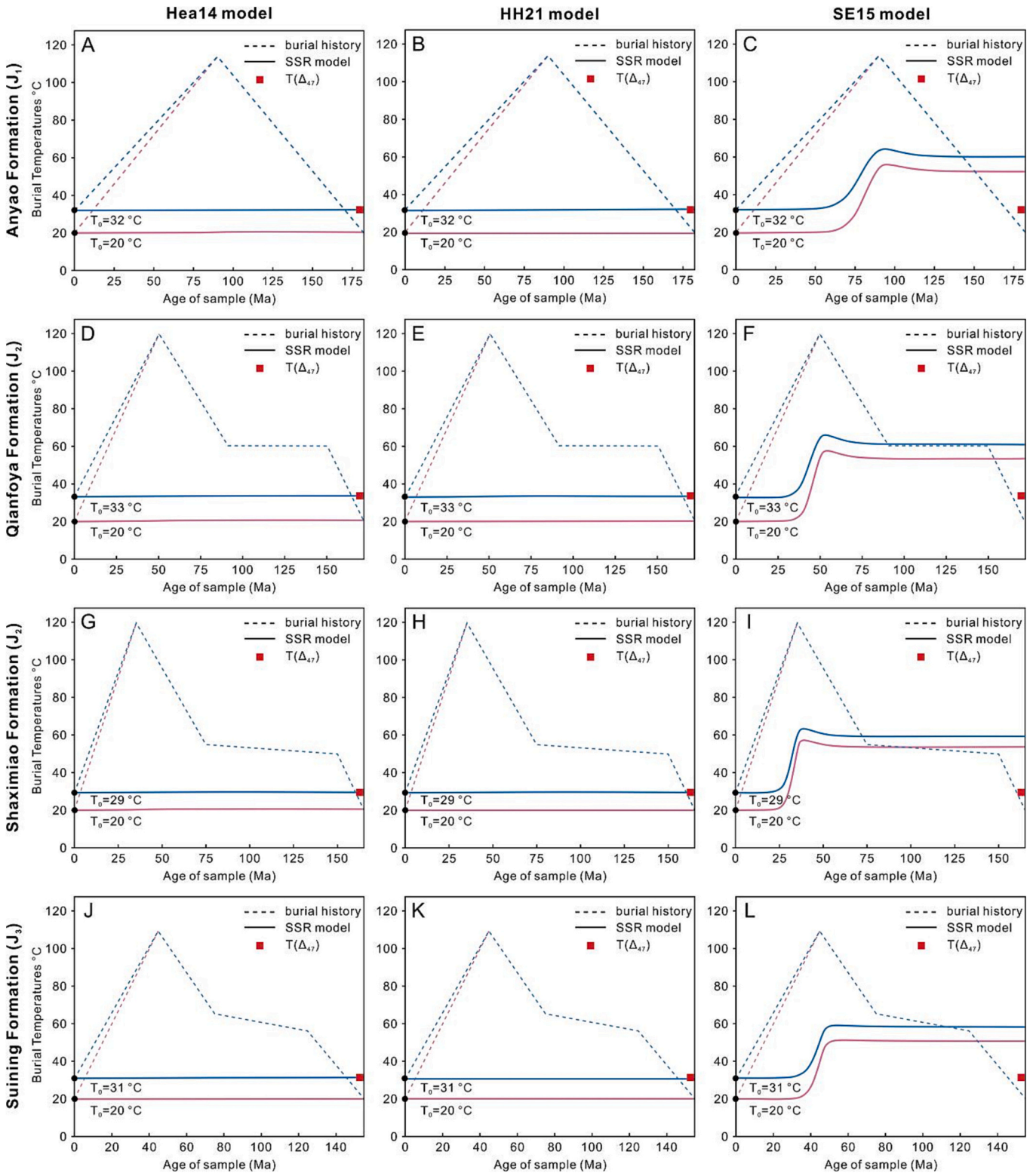

Fig. 4. Solid-state reordering modeling results for (A-C) the Anyao Formation in the Jiyuan Basin, (D—F) the Qianfoya Formation in the Zigui Basin, (G-I) the Shaximiao Formation in the Sichuan Basin, and (J-L) the Suining Formation in the Sichuan Basin. The reordering models come from Henkes et al. (2014) (Hea14 model), Stolper and Eiler (2015) (SE15 model), and Hemingway and Henkes (2021) (HH21 model), and they were performed using an open source "isotopylog" package (Hemingway, 2020; http://pypi.python.org/pypi/isotopylog). The thermal histories of these formations are inferred from Shi et al. (2016), Yu et al. (2017), and Zhao et al. (2002). Two cases of initial depositional temperature (T_0) are set as $T(\Delta_{47})$ values (blue lines) and 20 °C (pink lines). Additional models are shown in Supplemental Fig. S2. (For interpretation of the references to colour in this figure legend, the reader is referred to the web version of this article.)

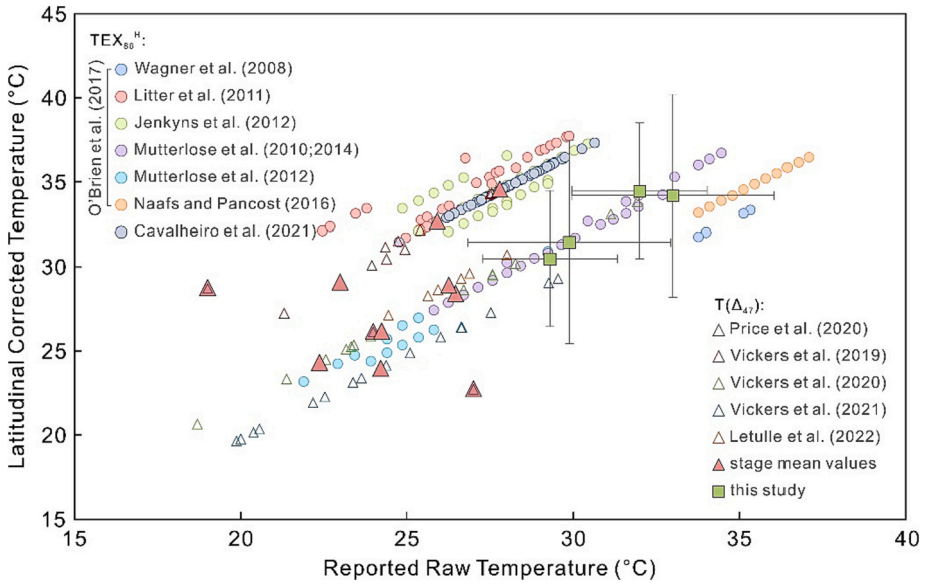

Fig. 5. The reported temperatures vs latitudinally corrected temperatures. All the temperatures are corrected to a common paleolatitude of 35° by applying a latitudinal temperature gradient of 0.4 ± 0.1 °C/°. Error bars represent 1 standard error (1SE).

Thus, our results from East China confirm a warm terrestrial paleoclimatic condition (i.e., 30 ± 4 °C to 34 ± 4 °C) at middle latitudes during the Middle Jurassic (Fig. 6A), which is ca. 10–15 °C higher than present. Importantly, our data show no evidence of a large cooling shift from the Early to Middle Jurassic accompanying the 4‰ increase in $\delta^{18}O$ over this interval (Fig. 6).

5.4. *No evidence of large temperature shifts during the Middle Jurassic-Earliest Cretaceous from SST and terrestrial records*

We next evaluate our terrestrial paleoproxy temperatures in light of previous SST reconstructions. To do this, the compiled contemporaneous SST estimates are also revised to 35° N/S latitude by applying a latitudinal temperature gradient of 0.4 ± 0.1 °C/° (Section 5.3; Fig. 5). During the period of overlap with our samples (approximately Callovian to Tithonian), this exercise leads to Δ_{47}-derived stage mean SSTs of 24–35 °C and TEX_{86}^{H}-derived SSTs of 32–37 °C (Figs. 5 and 6; Table S2). Our terrestrial mean annual paleotemperatures from low-paleoelevation basins are broadly consistent with these global SSTs, which bolsters our interpretation in Section 5.2 that there is no obvious seasonal bias for the nodule paleotemperatures. However, some discrepancies among the different terrestrial and marine temperature proxies remain.

The Δ_{47}-derived marine temperatures that reflect sea surface conditions at middle and high latitudes are statistically not different from our results (Fig. 6A), although they show relatively large variations that may be attributed to diverse physiological habitats of the different marine species in different locations (Vickers et al., 2020). In contrast, the SSTs derived from TEX_{86}^{H} are systematically ca. 3–4 °C warmer than our mean values (Fig. 6A). This result is consistent with previous studies that have noted that the TEX_{86}^{H} temperatures are generally higher than coeval $T(\Delta_{47})$ values during the Jurassic (Vickers et al., 2019) and other warm climate intervals (Meyer et al., 2018; Jones et al., 2022), indicating a potential warm bias in TEX_{86}^{H} temperatures.

We might expect to see a significant temperature increase over the Callovian to Tithonian based on the observed ca. 2‰ decrease in average belemnite $\delta^{18}O$ at this time (Fig. 6B). But despite the systematic offset between the TEX_{86}^{H}-derived SSTs and the clumped isotope derived SSTs and terrestrial temperatures, our data do not show obvious evidence of systematic warming at this time (Fig. 6A). This is in contrast to some other studies that have proposed significant temperature changes over parts of this time period, for example a cooling of ca. 5 °C during the Callovian-Oxfordian based on oxygen isotopes from middle latitudes in Northern Hemisphere (Dromart et al., 2003), and a few low SST estimates from TEX_{86} in South Atlantic during the Callovian (Jenkyns et al., 2012) (time periods of proposed cooling indicated with grey arrows in Fig. 6A). Additional records could help evaluate this interpretation given that large uncertainties in the clumped isotope-based estimates may permit significant temperature variation.

Examining our results together with the TEX_{86}^{H}-derived SSTs during the Late Jurassic enables us to evaluate the long-term paleoclimate evolution from the Middle Jurassic to Early Cretaceous (180–120 Ma) (Fig. 6A; Table S2). Taken together with the SST data, our new data filling the Middle Jurassic gap in paleotemperature estimates may be consistent with only modest temperature variations from the Early Jurassic to the Earliest Cretaceous. Our results and the LOESS fit of the TEX_{86}^{H}-based temperatures show a smoothed trend (34 ± 1 °C) that ranges from 30 to 36 °C during the Middle Jurassic-Early Cretaceous (Fig. 6A), with fluctuations in average temperature of ~6 °C appearing in the TEX_{86}^{H}-based estimates during the Valanginian and Hauterivian. During this period, the belemnite $\delta^{18}O$ curve shows dramatic variations, especially two cooling events with temperature variations of ca. 15 °C during the Middle Jurassic and Early Cretaceous (Grossman, 2012) (Fig. 6B). In contrast, our results indicate that the fluctuations of the mean annual temperatures are likely <4 °C throughout the Middle Jurassic, and not >10 °C after the errors are taken into account. Based on these observations, we suggest that the paleoclimatic conditions were relatively warm and stable from the Middle Jurassic to at least the Earliest Cretaceous, and highlight the importance of terrestrial paleotemperatures that provide another aspect to evaluate the global paleoclimate evolution.

5.5. *Coupling between global paleotemperature and pCO_2 levels*

We speculate that the stability of paleotemperatures, both on land and in oceans, may be related to relatively consistent pCO_2 levels during the Middle Jurassic and the Early Cretaceous. The pCO_2 values obtained from paleosol nodules in our study align with the global stomata-based pCO_2 levels and are also in agreement with the recalculated pCO_2 values from pedogenic carbonates (Fig. 6C). It is also worth noting that previous pCO_2 studies based on pedogenic carbonates generally reported lower pCO_2 values (Li et al., 2022a, 2022b), possibly due to assumptions of low paleosol formation temperatures.

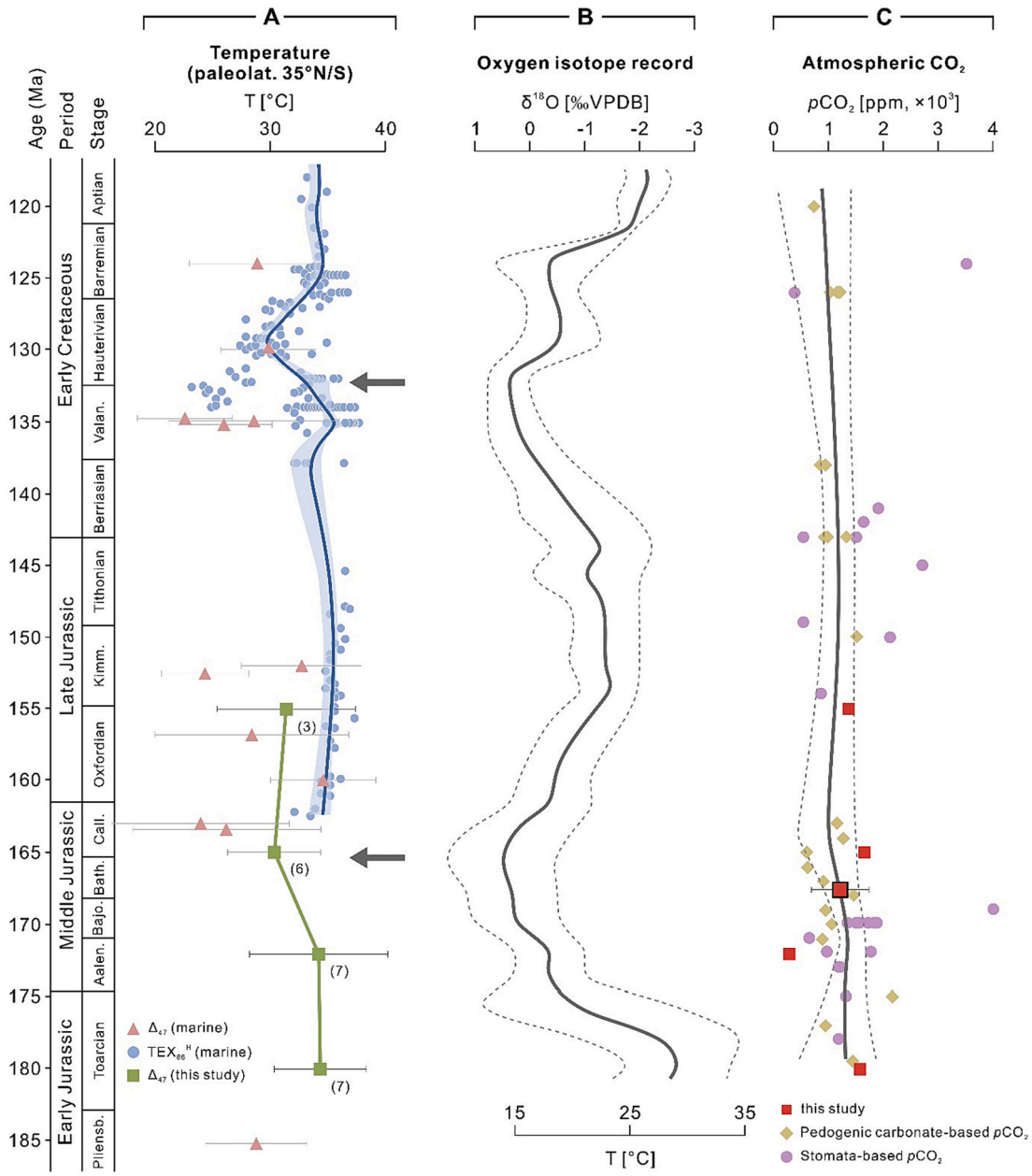

Fig. 6. Multiproxy paleotemperature records for the Jurassic-Early Cretaceous interval. (A) The paleotemperature record is based on our Δ_{47}-derived temperatures (green square) and compiled Δ_{47}-derived sea surface temperature (SSTs) (red triangles) and TEX_{86}^{H}-derived SSTs (blue dots). The smoothed curve (blue line) of TEX_{86}^{H}-derived SSTs is generated using locally weighted smoothing (LOESS) in PAST software. The blue shaded area represents a 95% confidence interval. Numbers of replicates are reported in parentheses. Error bars represent 1 standard error (1SE). (B) The belemnite $\delta^{18}O$-derived paleotemperature curve is modified from Grossman (2012). (C) The pCO_2 records are based on our paleosol nodules-based pCO_2 and compiled pCO_2 values based on pedogenic carbonates (yellow diamonds) and stomatal characters of fossil plants (purple circles). The smoothed curve (grey line) of all the compiled pCO_2 values is generated using locally weighted smoothing (LOESS) in PAST software. Error bars represent 1 standard error (1SE). (For interpretation of the references to colour in this figure legend, the reader is referred to the web version of this article.)

When comparing to pCO_2 levels during the Early Cretaceous, our results and the LOESS fit of the compiled pCO_2 values exhibit a gentle trend from the Middle Jurassic through to the Early Cretaceous (Fig. 6C). While there are limitations such as the shortage of global data and large age uncertainties that hinder our ability to identify specific pCO_2 perturbations, our curve provides valuable insights into the baseline pCO_2 levels during the Jurassic and the Early Cretaceous. Notably, the difference in average pCO_2 values during the Jurassic and the Early Cretaceous is <50 ppmv. This long-term pattern of pCO_2 stability spanning the Jurassic and the Early Cretaceous aligns with our predictions for paleotemperature during this interval. Consequently, our findings support the idea that pCO_2 levels have remained consistent with past global climate change patterns.

6. Conclusions

By applying clumped isotope paleothermometry to well-preserved paleosol carbonates in the central part of East China, we suggest that the mean annual temperatures in low-elevation, mid-latitude areas ranged from 30 ± 4 °C to 34 ± 4 °C (1 SE) during the Middle Jurassic. Our Δ_{47}-derived paleotemperatures are broadly consistent with coeval Δ_{47}-derived and TEX_{86}^{H}-derived sea surface temperatures, that together

indicate a relatively warm and stable paleoclimate during the Middle Jurassic to at least the Earliest Cretaceous (ca. 180–135 Ma). Furthermore, our estimate of pCO_2 during the Middle Jurassic is 1219 ± 519 ppmv, which is in agreement with coeval global pCO_2 records, showing minimal fluctuations when compared to the Early Cretaceous. These findings collectively indicate a connection between the stable paleotemperature records and the relatively constant pCO_2 levels from the Middle Jurassic through the Early Cretaceous.

Declaration of competing interest

The authors declare that they have no known competing financial interests or personal relationships that could have appeared to influence the work reported in this paper.

Data availability

The data used in this research are provided in the supplementary Materials

Acknowledgments

This study was financially supported by the National Natural Science Foundation of China (grant 41888101), the Chinese "111" project (grant B20011), and the Fundamental Research Funds for the Central Universities (grants 2652023001, 265202103 and 2652021093). This manuscript is a contribution to IGCP 739 project. We are grateful to the editor and two reviewers who provided instructive comments and suggestions and improved the quality of the manuscript.

Appendix A. Supplementary data

Supplementary data to this article can be found online at https://doi.org/10.1016/j.palaeo.2024.112014.

References

Amiot, R., Lécuyer, C., Buffetaut, E., Fluteau, F., Legendre, S., Martineau, F., 2004. Latitudinal temperature gradient during the Cretaceous Upper Campanian–Middle Maastrichtian: $\delta^{18}O$ record of continental vertebrates. Earth Planet. Sci. Lett. 226, 255–272.

Anderson, N.T., Kelson, J.R., Kele, S., Daeron, M., Bonifacie, M., Horita, J., Mackey, T.J., John, C.M., Kluge, T., Petschnig, P., Jost, A.B., Huntington, K.W., Bernasconi, S.M., Bergmann, K.D., 2021. A unified clumped isotope thermometer calibration (0.5–1,100 degrees C) using carbonate-based standardization. Geophys. Res. Lett. 48.

Arens, N.C., Jahren, A.H., Amundson, R., 2000. Can C3 plants faithfully record the carbon isotopic composition of atmospheric carbon dioxide? Paleobiol. 26, 137–164.

Banner, J.L., Hanson, G.N., 1990. Calculation of simultaneous isotopic and trace-element variations during water-rock interaction with applications to carbonate diagenesis. Geochim. Cosmochim. Acta 54, 3123–3137.

Berner, R.A., Kothavala, Z., 2001. GEOCARB III: a revised model of atmospheric CO2 over phanerozoic time. Am. J. Sci. 301, 182–204.

Breecker, D.O., Retallack, G.J., 2014. Refining the pedogenic carbonate atmospheric CO2 proxy and application to Miocene CO2. Palaeogeogr. Palaeoclimatol. Palaeoecol. 406, 1–8.

Burgener, L., Huntington, K.W., Hoke, G.D., Schauer, A., Ringham, M.C., Latorre, C., Diaz, F.P., 2016. Variations in soil carbonate formation and seasonal bias over > 4 km of relief in the western Andes (30 degrees S) revealed by clumped isotope thermometry. Earth Planet. Sci. Lett. 441, 188–199.

Cavalheiro, L., Wagner, T., Steinig, S., Bottini, C., Dummann, W., Esegbue, O., Gambacorta, G., Giraldo-Gomez, V., Farnsworth, A., Floegel, S., Hofmann, P., Lunt, D.J., Rethemeyer, J., Torricelli, S., Erba, E., 2021. Impact of global cooling on early cretaceous high pCO(2) world during the weissert event. Nat. Commun. 12.

Cerling, T., 1991. Carbon dioxide in the atmosphere: Evidence from cenozoic and mesozoic paleosols. Am. J. Sci. 291, 377–400.

Dai, X., Du, Y., Ziegler, M., Wang, C., Ma, Q., Chai, R., Guo, H., 2022. Middle triassic to late jurassic climate change on the northern margin of the South China plate: insights from chemical weathering indices and clay mineralogy. Palaeogeogr. Palaeoclimatol. Palaeoecol. 585.

Deng, S., Lu, Y., Zhao, Y., Fan, R., Wang, Y., Yang, X., Li, X., Sun, B., 2017. The Jurassic palaeoclimate regionalization and evolution of China. Earth Sci. Front. 24, 106–142 (in Chinese with English abstract).

Dennis, K.J., Affek, H.P., Passey, B.H., Schrag, D.P., Eiler, J.M., 2011. Defining an absolute reference frame for 'clumped' isotope studies of CO2. Geochim. Cosmochim. Acta 75, 7117–7131.

Dera, G., Brigaud, B., Monna, F., Laffont, R., Pucéat, E., Deconinck, J.F., Pellenard, P., Joachimski, M., Durlet, C., 2011. Climatic ups and downs in a disturbed Jurassic world. Geology 39, 215–218.

Dromart, G., Garcia, J.P., Picard, S., Atrops, F., Lécuyer, C., Sheppard, S.M.F., 2003. Ice age at the Middle–Late Jurassic transition? Earth Planet. Sci. Lett. 213, 205–220.

Eiler, J.M., 2007. "Clumped-isotope" geochemistry - The study of naturally-occurring, multiply-substituted isotopologues. Earth Planet. Sci. Lett. 262, 309–327.

Ekart, D.D., Cerling, T.E., Montanez, I.P., Tabor, N.J., 1999. A 400 million year carbon isotope record of pedogenic carbonate: implications for paleoatmospheric carbon dioxide. Am. J. Sci. 299, 805–827.

Fletcher, B.J., Brentnall, S.J., Anderson, C.W., Berner, R.A., Beerling, D.J., 2008. Atmospheric carbon dioxide linked with Mesozoic and early Cenozoic climate change. Nat. Geosci. 1, 43–48.

Gallagher, T.M., Sheldon, N.D., 2016. Combining soil water balance and clumped isotopes to understand the nature and timing of pedogenic carbonate formation. Chem. Geol. 435, 79–91.

Gao, Y., Zhang, S., Zhao, H., Ren, Q., Yang, T., Wu, H., Li, H., 2021. North China block underwent simultaneous true polar wander and tectonic convergence in late jurassic: new paleomagnetic constraints. Earth Planet. Sci. Lett. 567.

Ghosh, P., Adkins, J., Affek, H., Balta, B., Guo, W., Schauble, E.A., Schrag, D., Eller, J.M., 2006. C-13-O-18 bonds in carbonate minerals: A new kind of paleothermometer. Geochim. Cosmochim. Acta 70, 1439–1456.

Grossman, E.L., 2012. Chapter 10 - Oxygen Isotope Stratigraphy. In: Gradstein, F.M., Ogg, J.G., Schmitz, M.D., Ogg, G.M. (Eds.), The Geologic Time Scale. Elsevier, Boston, pp. 181–206.

Hemingway, J.D., 2020. Isotopylog: open-source tools for clumped isotope kinetic data analysis, 2020.

Hemingway, J.D., Henkes, G.A., 2021. A disordered kinetic model for clumped isotope bond reordering in carbonates. Earth Planet. Sci. Lett. 566.

Henkes, G.A., Passey, B.H., Grossman, E.L., Shenton, B.J., Perez-Huerta, A., Yancey, T.E., 2014. Temperature limits for preservation of primary calcite clumped isotope paleotemperatures. Geochim. Cosmochim. Acta 139, 362–382.

Huang, D., 2019. Jurassic integrative stratigraphy and timescale of China. Sci. China Earth Sci. 62, 223–255.

Huang, C., Retallack, G., Wang, C., 2012. Early Cretaceous atmospheric pCO2 levels recorded from pedogenic carbonates in China. Cretac. Res. 33, 42–49.

Huang, B., Yan, Y., Piper, J.D.A., Zhang, D., Yi, Z., Yu, S., Zhou, T., 2018. Paleomagnetic constraints on the paleogeography of the East Asian blocks during Late Paleozoic and Early Mesozoic times. Earth Sci. Rev. 186, 8–36.

Huber, B.T., MacLeod, K.G., Watkins, D.K., Coffin, M.F., 2018. The rise and fall of the Cretaceous Hot Greenhouse climate. Glob. Planet. Change 167, 1–23.

Huntington, K.W., Lechler, A.R., 2015. Carbonate clumped isotope thermometry in continental tectonics. Tectonophysics 647, 1–20.

Huntington, K.W., Petersen, S.V., 2023. Frontiers of Carbonate Clumped Isotope Thermometry. Annu. Rev. Earth Planet. Sci. 51, 611–641.

Ingalls, M., Snell, K.E., 2021. Tools for Comprehensive Assessment of Fluid-Mediated and Solid-State Alteration of Carbonates Used to Reconstruct Ancient Elevation and Environments. Front.Earth Sci. 9.

Jenkyns, H.C., Schouten-Huibers, L., Schouten, S., Damste, J.S.S., 2012. Warm Middle Jurassic-Early Cretaceous high-latitude sea-surface temperatures from the Southern Ocean. Clim. Past 8, 215–226.

Jin, X., Shi, Z., Baranyi, V., Kemp, D.B., Han, Z., Luo, G., Hu, J., He, F., Chen, L., Preto, N., 2020. The Jenkyns Event (early Toarcian OAE) in the Ordos Basin, North China. Glob. Planet. Change 193, 103273.

Joachimski, M.M., Mueller, J., Gallagher, T.M., Mathes, G., Chu, D.L., Mouraviev, F., Silantiev, V., Sun, Y.D., Tong, J.N., 2022. Five million years of high atmospheric CO2 in the aftermath of the Permian-Triassic mass extinction. Geology 50, 650–654.

Jones, M.M., Petersen, S.V., Curley, A.N., 2022. A tropically hot mid-Cretaceous North American Western Interior Seaway. Geology 50, 954–958.

Kelson, J.R., Huntington, K.W., Schauer, A.J., Saenger, C., Lechler, A.R., 2017. Toward a universal carbonate clumped isotope calibration: Diverse synthesis and preparatory methods suggest a single temperature relationship. Geochim. Cosmochim. Acta 197, 104–131.

Kelson, J.R., Huntington, K.W., Breecker, D.O., Burgener, L.K., Gallagher, T.M., Hoke, G. D., Petersen, S.V., 2020. A proxy for all seasons? A synthesis of clumped isotope data from Holocene soil carbonates. Quat. Sci. Rev. 234, 106259.

Kim, S.T., Oneil, J.R., 1997. Equilibrium and nonequilibrium oxygen isotope effects in synthetic carbonates. Geochim. Cosmochim. Acta 61, 3461–3475.

Kim, J.H., van der Meer, J., Schouten, S., Helmke, P., Willmott, V., Sangiorgi, F., Koç, N., Hopmans, E.C., Damsté, J.S.S., 2010. New indices and calibrations derived from the distribution of crenarchaeal isoprenoid tetraether lipids: Implications for past sea surface temperature reconstructions. Geochim. Cosmochim. Acta 74, 4639–4654.

Letulle, T., Suan, G., Daeron, M., Rogov, M., Lecuyer, C., Vincon-Laugier, A., Reynard, B., Montagnac, G., Lutikov, O., Schlogl, J., 2022. Clumped isotope evidence for Early Jurassic extreme polar warmth and high climate sensitivity. Clim. Past 18, 435–448.

Li, S., Zhao, G., Dai, L., Liu, X., Zhou, L., Santosh, M., Suo, Y., 2012. Mesozoic basins in eastern China and their bearing on the deconstruction of the North China Craton. J. Asian Earth Sci. 47, 64–79.

Li, Y., He, D., Li, D., Lu, R., Fan, C., Sun, Y., Huang, H., 2018. Sedimentary provenance constraints on the Jurassic to Cretaceous paleogeography of Sichuan Basin, SW China. Gondwana Res. 60, 15–33.

Li, X., Wang, J., Rasbury, T., Zhou, M., Wei, Z., Zhang, C., 2020. Early Jurassic climate and atmospheric CO2 concentration in the Sichuan paleobasin, southwestern China. Clim. Past 16, 2055–2074.
Li, X., Hu, Y., Guo, J., Lan, J., Lin, Q., Bao, X., Yuan, S., Wei, M., Li, Z., Man, K., Yin, Z., Han, J., Zhang, J., Zhu, C., Zhao, Z., Liu, Y., Yang, J., Nie, J., 2022a. A high-resolution climate simulation dataset for the past 540 million years. Sci. Data 9, 371.
Li, J., Huang, C.-M., Yang, G.-L., Pan, Y.-Y., Wen, X.-Y., 2022b. Middle Jurassic climate oscillations from paleosol records of the Sichuan Basin, SW China. J. Palaeogeogr. 11, 97–122.
Liu, S., Steel, R., Zhang, G., 2005. Mesozoic sedimentary basin development and tectonic implication, northern Yangtze Block, eastern China: record of continent - continent collision. J. Asian Earth Sci. 25, 9–27.
Meng, Q., Wang, E., Hu, J., 2005. Mesozoic sedimentary evolution of the northwest Sichuan basin: Implication for continued clockwise rotation of the South China block. Geol. Soc. Am. Bull. 117, 396–410.
Meng, Q., Wu, G., Fan, L., Wei, H., 2019. Tectonic evolution of early Mesozoic sedimentary basins in the North China block. Earth Sci. Rev. 190, 416–438.
Meyer, K.W., Petersen, S.V., Lohmann, K.C., Winkelstern, I.Z., 2018. Climate of the Late Cretaceous North American Gulf and Atlantic Coasts. Cretac. Res. 89, 160–173.
O'Brien, C.L., Robinson, S.A., Pancost, R.D., Sinninghe Damsté, J.S., Schouten, S., Lunt, D.J., Alsenz, H., Bornemann, A., Bottini, C., Brassell, S.C., Farnsworth, A., Forster, A., Huber, B.T., Inglis, G.N., Jenkyns, H.C., Linnert, C., Littler, K., Markwick, P., McAnena, A., Mutterlose, J., Naafs, B.D.A., Püttmann, W., Sluijs, A., van Helmond, N.A.G.M., Vellekoop, J., Wagner, T., Wrobel, N.E., 2017. Cretaceous sea-surface temperature evolution: Constraints from TEX 86 and planktonic foraminiferal oxygen isotopes. Earth Sci. Rev. 172, 224–247.
Passey, B.H., Levin, N.E., Cerling, T.E., Brown, F.H., Eiler, J.M., 2010. High-temperature environments of human evolution in East Africa based on bond ordering in paleosol carbonates. Proc. Natl. Acad. Sci. 107, 11245–11249.
Peters, N.A., Huntington, K.W., Hoke, G.D., 2013. Hot or not? Impact of seasonally variable soil carbonate formation on paleotemperature and O-isotope records from clumped isotope thermometry. Earth Planet. Sci. Lett. 361, 208–218.
Petersen, S.V., Defliese, W.F., Saenger, C., Daeron, M., Huntington, K.W., John, C.M., Kelson, J.R., Bernasconi, S.M., Colman, A.S., Kluge, T., Olack, G.A., Schauer, A.J., Bajnai, D., Bonifacie, M., Breitenbach, S.F.M., Fiebig, J., Fernandez, A.B., Henkes, G. A., Hodell, D., Katz, A., Kele, S., Lohmann, K.C., Passey, B.H., Peral, M.Y., Petrizzo, D.A., Rosenheim, B.E., Tripati, A., Venturelli, R., Young, E.D., Winkelstern, I.Z., 2019. Effects of Improved O-17 Correction on Interlaboratory Agreement in Clumped Isotope Calibrations, Estimates of Mineral-Specific Offsets, and Temperature Dependence of Acid Digestion Fractionation. Geochem. Geophys. Geosyst. 20, 3495–3519.
Price, G.D., Twitchett, R.J., Wheeley, J.R., Buono, G., 2013. Isotopic evidence for long term warmth in the Mesozoic. Sci. Rep. 3, 1438.
Price, G.D., Bajnai, D., Fiebig, J., 2020. Carbonate clumped isotope evidence for latitudinal seawater temperature gradients and the oxygen isotope composition of Early Cretaceous seas. Palaeogeogr. Palaeoclimatol, Palaeoecol, p. 552.
Retallack, G.J., 2001. Soils of the Past–An Introduction to Paleopedology. Blackwell Science Ltd, Oxford, UK, p. 333.
Retallack, G.J., 2009. Greenhouse crises of the past 300 million years. Geol. Soc. Am. Bull. 121, 1441–1455.
Romanek, C.S., Grossman, E.L., Morse, J.W., 1992. Carbon isotopic fractionation in synthetic aragonite and calcite: effects of temperature and precipitation rate. Geochim. Cosmochim. Acta 56, 419–430.
Schauer, A.J., Kelson, J., Saenger, C., Huntington, K.W., 2016. Choice of O-17 correction affects clumped isotope (Delta(47)) values of CO2 measured with mass spectrometry. Rapid Commun. Mass Spectrom. 30, 2607–2616.
Scotese, C., 2014. Atlas of Jurassic Paleogeographic Maps, PALEOMAP Atlas for ArcGIS. In: The Jurassic and Triassic, Maps 32–42, Mollweide Projection, PALEOMAP Project, Evanston, IL, vol. 3.
Shen, H., Zhang, L., Wang, C., Amiot, R., Wang, X., Cui, L., Song, P., 2021. Early Jurassic palaeoclimate in Southwest China and its implications for dinosaur fossil distribution. Geol. J. 56, 6245–6258.
Shi, H., Shi, X., Glasmacher, U.A., Yang, X., Stockli, D.F., 2016. The evolution of eastern Sichuan basin, Yangtze block since Cretaceous: Constraints from low temperature thermochronology. J. Asian Earth Sci. 116, 208–221.
Stolper, D.A., Eiler, J.M., 2015. The kinetics of solid-state isotope-exchange reactions for clumped isotopes: A study of inorganic calcites and apatites from natural and experimental samples. Am. J. Sci. 315, 363.
Sun, B., Xiao, L., Xie, S., Deng, S., Wang, Y., Jia, H., Turner, S., 2007. Quantitative Analysis of Paleoatmospheric CO2 Level Based on Stomatal Characters of Fossil Ginkgo from Jurassic to Cretaceous in China. Acta Geol. Sin. 81, 931–939.
van Hinsbergen, D.J.J., de Groot, L.V., van Schaik, S.J., Spakman, W., Bijl, P.K., Sluijs, A., Langereis, C.G., Brinkhuis, H., 2015. A Paleolatitude Calculator for Paleoclimate Studies. PloS One 10.
Vickers, M.L., Bajnai, D., Price, G.D., Linckens, J., Fiebig, J., 2019. Southern high-latitude warmth during the Jurassic–Cretaceous: New evidence from clumped isotope thermometry. Geology 47, 724–728.
Vickers, M.L., Fernandez, A., Hesselbo, S.P., Price, G.D., Bernasconi, S.M., Lode, S., Ullmann, C.V., Thibault, N., Hougaard, I.W., Korte, C., 2020. Unravelling middle to late jurassic palaeoceanographic and palaeoclimatic signals in the hebrides basin using belemnite clumped isotope thermometry. Earth Planet. Sci. Lett. 546.
Vickers, M.L., Bernasconi, S.M., Ullmann, C.V., Lode, S., Looser, N., Morales, L.G., Price, G.D., Wilby, P.R., Hougard, I.W., Hesselbo, S.P., Korte, C., 2021. Marine temperatures underestimated for past greenhouse climate. Sci. Rep. 11.
Wang, Y., 2002. Fern ecological implications from the Lower Jurassic in Western Hubei, China. Rev. Palaeobot. Palynol. 119, 125–141.
Wang, C., Scott, R.W., Wan, X., Graham, S.A., Huang, Y., Wang, P., Wu, H., Dean, W.E., Zhang, L., 2013. Late Cretaceous climate changes recorded in Eastern Asian lacustrine deposits and North American Epieric sea strata. Earth Sci. Rev. 126, 275–299.
Wang, M., Guo, W., Yang, W., 2019. Detrital zircon trace elements from the Mesozoic Jiyuan Basin, central China and its implication on tectonic transition of the Qinling Orogenic Belt. Open Geosci. 11, 125–139.
Wu, J., Ding, S., Li, Q., Sun, B., Wang, Y., 2016. Reconstructing paleoatmospheric CO2 levels based on fossil Ginkgoites from the Upper Triassic and Middle Jurassic in Northwest China. PalZ 90, 377–387.
Yan, D., Sun, B., Xie, S., Li, X., Wen, W., 2009. Response to paleoatmospheric CO2 concentration of Solenites vimineus (Phillips) Harris (Ginkgophyta) from the Middle Jurassic of the Yaojie Basin, Gansu Province, China. Sci. China Ser. D Earth Sci. 52, 2029–2039.
Yang, W., Yang, J., Wang, X., Du, Y., 2014. Uplift-denudation history of the Qinling orogen: Constrained from the detrital-zircon U–Pb geochronology. J. Asian Earth Sci. 89, 54–65.
Yu, W., Shen, C., Yang, C., 2017. Constraints of fission track dating on the Mesozoic-Cenozoic tectonic-thermal evolution of the Zigui Basin. Earth Sci. Front. 24, 116–126 (in Chinese with English abstract).
Zhang, L., Wang, C., Wignall, P.B., Kluge, T., Wan, X., Wang, Q., Gao, Y., 2018. Deccan volcanism caused coupled pCO(2) and terrestrial temperature rises, and pre-impact extinctions in northern China. Geology 46, 271–274.
Zhang, L., Hay, W.W., Wang, C., Gu, X., 2019. The evolution of latitudinal temperature gradients from the latest Cretaceous through the Present. Earth Sci. Rev. 189, 147–158.
Zhang, Q., Gong, E., Zhang, Y., Guan, C., 2021. Early Jurassic (Toarcian) warming identified from lacustrine sediments of eastern Liaoning, China. Geol. Mag. 158, 1194–1208.
Zhao, W., Jin, Q., Wang, W., 2002. Estimation of ancient subsurface temperatures with the apatite fission tracks in Jiyuan depression, North China Basin. Pet. Geol. Exp. 24, 555–560 (in Chinese with English abstract).